



Contents lists available at ScienceDirect

Geomechanics for Energy and the Environment

journal homepage: www.elsevier.com/locate/gete

Coupled CFD–DEM numerical modelling of perforation damage and sand production in weak sandstone formation

Furkhat Khamitov^{a,*}, Nguyen Hop Minh^b, Yong Zhao^a^a Nazarbayev University, Nur-Sultan 010000, Kazakhstan^b Fulbright University Vietnam, Ho Chi Minh City 700000, Viet Nam

ARTICLE INFO

Article history:

Received 30 May 2020

Received in revised form 17 February 2021

Accepted 3 May 2021

Available online xxx

Editors-in-Chief:

Professor Lyesse Laloui and Professor Tomasz Hueckel

Keywords:

DEM

Plastic

Elastic

CFD–DEM

Cement

Sand production

ABSTRACT

A coupled microscopic simulation method was implemented to investigate the bond breakage behaviour during perforation and sand production in a weak cemented sandstone. A new contact bond model was implemented in the open-source program CFDEM to simulate a large cylindrical sample of one hundred thousand numerical particles using a high-performance computer (HPC) system. The coupled simulation of the particle–fluid phases and the information exchange between them required intensive computational power and highly efficient parallelization algorithms, yet it provided the detailed information on the distribution of bond and bond breakage, new contact formation, particle migration and the associated change in the internal porosity across the sample. The perforation process was found to create a damage zone that contained a compacted core of unbonded particles. The compacted core expanded quickly under fluid flow condition and released its particles to migrate towards the perforation tunnel. Small particles were produced first from the perforation damage zone, while fewer particles of larger sizes were produced later in an overall transient sand production phenomenon.

© 2021 Elsevier Ltd. All rights reserved.

1. Introduction

Sand production is one of the important factors associated with the shallow heavy oil reservoirs. The produced sands can damage equipment, increase operational cost, and affect production schedule, which may give rise to critical failure of wells.¹ On the other hand, as sand is produced from the reservoir, it creates a zone of enhanced permeability that allows a greater fluid flux to the wellbore.^{2,3} Sand production can be characterized as a two-stage process. In the first stage, the weak rock materials fail under the local stress condition, while in the second stage, sand particles from the failure zone can be transported out from the perforation by the fluid flow. Perforation of the formation redistributes the stresses around the perforation tunnel and is directly related to the creation of a damage zone. Sand production can be classified as three types: transient, continuous and catastrophic sand production.⁴ The transient sand production describes a decreasing pattern of the produced sand mass with time under a constant well production condition. The continuous sand production occurs when sand is produced constantly. The catastrophic sand production refers to events where a high rate of sand influx causes the well suddenly chokes and/or dies.

The perforation process can damage the reservoir rock and reduce productivity of oil wells. This is caused by clogging of perforation tunnel by crushed rock, which affects the porosity and permeability in the local areas near to the well.^{5,6} In unconsolidated sands, the perforation guns do not create an ideal “tunnel or cavity” in the formation but rather a perforation zone that is filled with crushed formation materials and debris.⁷

Due to the complex interactions between the solid phase and the fluid phase, the sand production phenomenon has been investigated using different numerical methods that are mainly placed under two categories: the continuum and discrete particle approaches.⁸ In the continuum approach, materials are treated as continuous in deriving the governing differential equations. The most common and simplest model for rock failure and wellbore stability analysis is the linear elastic model. An important advantage of the linear elastic model is in the small number of input parameters and the low computational power requirement for the calculation of these models.⁹ The more advanced elastoplastic constitutive models, however, help to distinguish between the recoverable and irrecoverable deformations for a better understanding of the stress–strain behaviour of the reservoir materials during loading and unloading.¹⁰

The assumption of continuity implies that the material cannot be separated or broken into smaller pieces. The deformation along or across a discontinuity (if any) is the same as the rest of the continuum.¹¹ The continuum approach hence could not

* Corresponding author.

E-mail address: Furkhat.khamitov@nu.edu.kz (F. Khamitov).

study local discontinuous phenomena such as the detachment of individual particles from the rock matrix. The particle approach as the Discrete Element Method is more capable to study the microscopic behaviour of the sand production in a bottom-up approach.¹²

The reservoir material can be modelled in the DEM simulation as an assembly of bonded particles in a computational domain. The particles can be tracked individually, explicitly during the simulation in order to provide each individual particle's trajectory. The coupled modelling between the particle phase and the fluid phase in a sand production simulation was first introduced by Tsuji et al. (1993), where the coupled DEM and Computational Fluid Dynamics (CFD) simulation was utilized to study the motion of particles in a two-dimensional gas-fluidized bed.¹³

O'Connor et al. (1997) introduced the application of DEM to model the mechanics of sand production. The 2D numerical simulation combined the Darcy flow model with DEM. The Darcy's law is only valid for slow (small Reynolds number), viscous and isothermal flow, the conditions that may not be met during all sand production stages.^{14,15} Cheung (2010) used a coupled (1D) fluid - (3D) DEM model to investigate the effect of fluid flow on sand production. The radial fluid flow, which was described by the Navier–Stokes equations, was injected from the outer boundary of a cylindrical sample to an inner perforation hole. Due to the simplification in the fluid model (1D), the drag force was only applied in one direction which does not truly represent the real-life conditions. The effect of particles on fluid flow was not taken into account in this study.¹⁶

Zhou et al. (2011) employed a coupled simulation of the (3D) DEM and the (3D) CFD models and showed that the main features of sand erosion in weak formation can be captured by the coupled CFD–DEM approach. It was concluded that the particle–fluid interaction force is the main driving force for sand erosion.¹⁷ A significant limitation of this study is however the use of only one layer of sand grains in the vertical direction. Climent (2016) used a three-dimensional coupled simulation, where the CFD model was based on the Navier–Stokes equations. The parallel-bond model was used to simulate the strong cement bonds between particles.^{18,19} The higher fluid flow velocity was found to create a larger plastic zone and a higher sand production rate.

Rakhimzhanova et al. (2018) developed a simple contact bond model based on the JKR's theory²⁰ to simulate the behaviour of a weak sandstone in Kazakhstan, which was found to have good agreement with experimental measurements. The model was utilized in further development to study the perforation and sand production of the same material,^{21,22} where a 3D coupled CFD–DEM model with the Immersed Boundary Method (IBM) was used in a simulation using 10,000 particles in a rectangular parallelepiped computational space.

In this study, we conducted a coupled 3D CFD–DEM simulation using the open-source program CFDEM²³ with a large numerical sample of 10^5 particles. The modified JKR model²⁴ was first implemented in the DEM program LIGGGHTS,²⁵ which was later combined with the CFD program OpenFOAM²⁶ for the study of the perforation damage and sand production of a weak sandstone material in Kazakhstan. We also improve upon the numerical studies by Rakhimzhanova et al. (2018, 2019, 2020) in terms of a more comparable cylindrical geometry instead of the parallelepiped geometry in the previous studies, a larger simulation scale, different flow directions and of the multiphase flow simulation that is an on-going research, as well as the detailed scientific visualization similar to Climent et al. (2014) to provide greater insight into the complex sanding processes.²⁷ Based on this visualization, the formation of a plastic zone due to perforation and how it evolves during sand production were investigated. A cylindrical geometry was selected for both the solid particle

phase and the fluid phase to be comparable to the experimental study of the same material.^{28,29} The radial water flow was injected towards the central vertical perforation and discrete particles were produced with the flow that was dependent on the applied solid stress and fluid pressure conditions. The creation of a perforation damage zone and how it evolved during sand production process were captured in the simulation and discussed in this paper.

2. Numerical formulation

2.1. DEM modelling of weak sandstone

The Discrete Element Method (DEM) was introduced by Cundall and Strack (1979) to study the microscopic behaviour of granular materials where the particles in the computational domain interact with each other as they are subjected to the boundary conditions. The locations of the particles in each simulation time step are tracked by explicitly solving the second Newton's law in term of the contact forces acting on each and every particle and using the particle's mass to find the acceleration value. The acceleration allows the calculation of the particle trajectory in each time step that provides an update on the number of contacts and contact forces that the particle develops with its neighbouring particles at the new location. Summing the updated contact forces provides the unbalanced force to calculate the corresponding particle's acceleration in the next time step. In a saturated system of particles immersed in a fluid (or fluid flow), the DEM simulation of the particle phase can be coupled with the Computational Fluid Dynamics (CFD) simulation of the fluid phase such that the calculation of the forces acting on a particles would include the fluid dynamical forces and the general second Newton's law for a particle p in this case can be given as follows²³:

$$\mathbf{m}_p \frac{d\mathbf{u}_p}{dt} = \mathbf{F}_{p,n} + \mathbf{F}_{p,t} + \mathbf{F}_{p,f} + \mathbf{F}_{p,p} + \mathbf{F}_{p,vis} + \mathbf{F}_{p,b}, \quad (1)$$

$$\mathbf{I}_p \frac{d\boldsymbol{\omega}_p}{dt} = \mathbf{r}_{p,c} \times \mathbf{F}_{p,t}, \quad (2)$$

where \mathbf{u}_p is linear and $\boldsymbol{\omega}_p$ -angular velocities, \mathbf{I}_p – moment of inertia, \mathbf{m}_p -mass, $\mathbf{r}_{p,c}$ -radius of the particle. $\mathbf{F}_{p,n}$ and $\mathbf{F}_{p,t}$ are the normal and tangential contact forces between particles, respectively; $\mathbf{F}_{p,f}$ is the drag force exerted from the fluid phase to the particle; $\mathbf{F}_{p,p}$ is pressure force, $\mathbf{F}_{p,vis}$ is viscous force, $\mathbf{F}_{p,b}$ are other forces affecting the particles.

The pressure force $\mathbf{F}_{p,p}$ can be calculated as:

$$\mathbf{F}_{p,p} = -\nabla P \cdot V_p \quad (3)$$

where V_p is volume of particle and ∇P is the fluid pressure gradient.

The viscous force $\mathbf{F}_{p,vis}$ can be calculated as:

$$\mathbf{F}_{p,vis} = -(\nabla \cdot \boldsymbol{\tau}) V_p. \quad (4)$$

where $\boldsymbol{\tau}$ is the fluid stress tensor (see Eq. (11)).

The Eq. (1) is used to describe the translational motion, while Eq. (2) is used for the rotational motion of the particle. Note that for dry materials, the fluid-related force terms are equal to zero. The particle–particle contact forces can be specified by different contact models, the implementation of which varies among different simulation codes and programs.^{30,31} In this study, we employed the open-source program LIGGGHTS²⁵ for the particle phase simulation, while the fluid phase is simulated by another open-source program OpenFOAM²⁶. The formulation of the particle phase is described in this section. The formulation of the fluid phase and the interaction between particles and fluid are described in the next section.

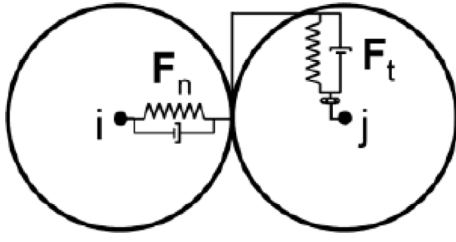


Fig. 1. Spring-dashpot model.²⁵

In LIGGGHTS, the spring-dashpot model was implemented (Fig. 1). The normal force is given by:

$$F_{p,n} = -k_{p,n}\delta_p + c_{p,n}\Delta u_{p,n} \quad (5)$$

where $F_{p,n}$ is the normal contact force of the particle as given in Eq. (1); $\Delta u_{p,n}$ is the normal relative velocity at the contact point; $k_{p,n}$ and $c_{p,n}$ are the normal spring stiffness and damping coefficient; δ_p is the normal overlap that for two particles i and j can be define as:

$$\delta_p = R_i + R_j - d \quad (6)$$

where R_i , R_j are the radii of particle i and j , respectively; d is the distance between the particles' centres.

The tangential force can be written as:

$$F_{p,t} = \min \left\{ \left| k_{p,t} \int_{t_{c,0}}^t \Delta u_{p,t} dt + c_{p,t} \Delta u_{p,t} \right|, \mu_c F_{p,n} \right\} \quad (7)$$

where $\Delta u_{p,t}$ is the relative tangential velocity of the particles in contact as given in Eq. (1); $k_{p,t}$ and $c_{p,t}$ are the tangential spring stiffness and the tangential damping coefficient; μ_c is the Coulomb coefficient of friction. The integral term represents an accumulated spring energy from the relative tangential motion between two particles in contact since the time of contact formation $t_{c,0}$ until the current time, t . The magnitude of the tangential force is limited by the Coulomb frictional limit, where the particles begin to slide over each other.

The interaction between particles is dependent, among others, on the material properties, the radii of the particles, the surface properties, the range of deformation. The behaviour can be approximated by different linear and non-linear, elastic and elasto-plastic constitutive models. The Hertz's theory³² was often used to describe the contact behaviour between unbonded particles (i.e. non-adhesive contact) where there is zero resistance to tensile force that separates particles along the radial direction. For the two particles i and j in Fig. 1, the normal stiffness k_n in Eq. (5) can be given as a function of the Young's modulus Y_i , Y_j and the Poisson's ratio ν_i , ν_j of the two particles in contact (assuming that they are made of different materials) as:

$$k_{p,n} = \frac{4}{3} Y^* \sqrt{R^* \delta_p} \quad (8)$$

$$\text{Where } Y^* = \frac{Y_i Y_j}{Y_j (1 - \nu_i^2) + Y_i (1 - \nu_j^2)} \text{ and } R^* = \frac{R_i R_j}{R_i + R_j}.$$

For auto-adhesive contact due to the Van der Waals forces between silt sized particles, the behaviour can be described by the JKR theory.²⁰ For small finite particle sizes,³¹ van der Waals forces become significant and particles tend to adhere to each other. The relationship between the normal contact force and the normal overlap as given by the JKR contact model is presented by the curve in Fig. 2. When the two particles approach each other, they are adhered to each other, which is presented by a jump in the value of $F_{p,n}$ from point O to point A in Fig. 2. Note that $F_{p,n}$ is negative at point A as it is a tensile force. As

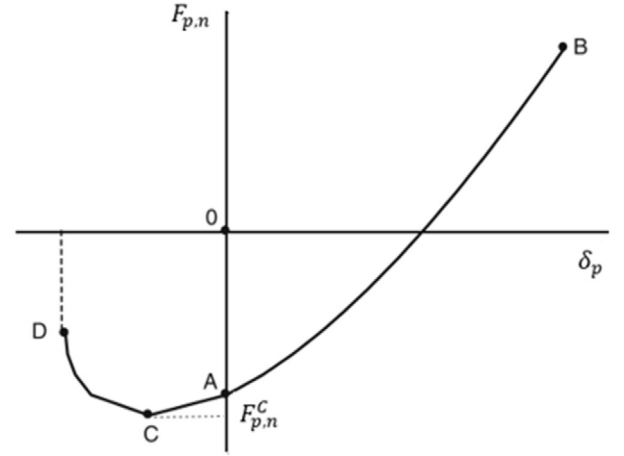


Fig. 2. Normal contact force vs overlap.³¹

two particles overlap each other between point A and point B, the curve presents a loading behaviour as $F_{p,n}$ increases with the value of the normal overlap δ_p . This behaviour can be given in the following equation²⁰:

$$(\delta_p R^*)^{3/2} = \frac{3}{4} R^* Y^* \left(F_{p,n} + 3\gamma\pi R^* + \sqrt{(6\gamma\pi R^* F_{p,n} + (3\gamma\pi R^*)^2)} \right) \quad (9)$$

where γ is interface energy, other parameters have been defined in previous equations.

Unloading may happen from F_B to F_A when the normal force decreases with the overlap. As the unloading curve passes point A, the two particles are separated by a negative overlap value, the tensile force continues to a maximum value $F_{p,n}^C$ at point C. That is defined as $F_{p,n}^C = 1.5\pi\gamma R^*$. The two particles are still bonded by a tensile resistance until the contact bond finally breaks at point D. If the interface energy, γ , is zero, the JKR model reverts to the Hertz equation.

The JKR model was modified by Rakhimzhanova et al. (2018) for the simulation of a weak cemented sandstone in Kazakhstan. In this work, there are two assumptions, first the bond breakage was set at point C instead of point D, which implies a less flexible bonding behaviour. Secondly, the bonds were assumed to form only once at the beginning of the simulation when the DEM sandstone was assumed in its intact state and the modified JKR model was used at this step. During subsequent loading conditions, the bonds broke and the particles formed new contacts. The newly formed contacts were not bonded and hence its behaviour was described by the Hertz model. The particle size in this study varies from 0.15 to 0.355 mm, however, numerical results of this approach are found to be in good agreement with experimental data.³³ Therefore, we continue to use this model in our study.

In this study, we adopted the same contact model by Rakhimzhanova et al. (2018) for the similar sandstone material and implement it in LIGGGHTS. The implementation was done in two steps, first to implement the original JKR model as it was not included in LIGGGHTS and then introduce the new bond breakage condition at point C and the transformation from the modified JKR model to the Hertz model once there is a bond breakage event occurs. The implementation was done successfully and the simulation results were verified with theoretical solutions.³⁴ Here, we extend the work further by utilizing the CFD-DEM simulation of the new contact model for the simulation of sand production from the weak sandstone.

2.2. Coupled CFD– DEM modelling of fluid–particle interaction

For the coupled CFD–DEM simulation in this study, the fluid phase is simulated as a continuum, while the solid phase is simulated as discrete particles (i.e. discontinuum modelling). The solid phase is fully resolvable, where each particle is tracked in the system throughout the simulation. The unresolved approach,³⁵ on the other hand, is used for the CFD simulation as the particle sizes are smaller than the computational grid of the fluid phase. Individual particles do not completely fill a computational fluid cell. This is different to the cases where the fluid cells are much smaller than the particle sizes and the interfaces between the two phases are the resolved surfaces in the CFD–DEM simulation.

In this paper we follow the CFD–DEM formulations of so-called model A, that recommend CFD–DEM modelling of complex particle–fluid flow. The governing equations that describe the motion of a fluid phase in the presence of a secondary particulate phase can be given by a modified set of the Navier–Stokes equations as follows³⁶:

$$\begin{cases} \frac{\partial(\varepsilon_f)}{\partial t} + \nabla \cdot (\varepsilon_f \mathbf{u}_f) = 0, \\ \frac{\partial(\varepsilon_f \rho_f \mathbf{u}_f)}{\partial t} + \nabla \cdot (\varepsilon_f \rho_f \mathbf{u}_f \mathbf{u}_f) = -\varepsilon_f \nabla P - \mathbf{F}_{pf}^{setll} + \varepsilon_f \nabla \cdot \boldsymbol{\tau} + \varepsilon_f \rho_f \mathbf{g}, \end{cases} \quad (10)$$

where ε_f is the volume fraction occupied by the fluid, \mathbf{u}_f – fluid velocity, ρ_f the fluid density, P the pressure, \mathbf{F}_{pf}^{setll} – volumetric particle–fluid interaction force, \mathbf{g} the gravity vector and t the time. The $\boldsymbol{\tau}$ – stress tensor, that for fluid with viscosity μ_f is calculated as:

$$\boldsymbol{\tau} = \mu_f [(\nabla \mathbf{u}_f) + (\nabla \mathbf{u}_f)^T] \quad (11)$$

The volumetric particle–fluid interaction force \mathbf{F}_{pf}^{setll} determine by:

$$\mathbf{F}_{pf}^{setll} = \frac{1}{\Delta V} \sum_{p=1}^n (\mathbf{f}_{p,f}) \quad (12)$$

$$\mathbf{f}_{p,f} = \mathbf{f}_{p,d} + \mathbf{f}_p'' \quad (13)$$

where ΔV – volume of fluid cell, n is a number of particles in computational cell, $\mathbf{f}_{p,f}$ is particle–fluid interaction force in Eq. (1); $\mathbf{f}_{p,d}$ – a drag force and \mathbf{f}_p'' is the sum of particle–fluid interaction forces on particles other than the drag, which are related to pressure gradient and viscous stress and are often regarded as the dominant forces in particle–fluid flow.

The drag force is based on the Di Felice correlation³⁷:

$$\mathbf{f}_{p,d} = 0.125 C_{d0,p} \rho_f \pi d_p^2 \varepsilon_p^2 |u_f - u_p| (u_f - u_p) \varepsilon_p^{-\chi} \quad (14)$$

where unknown χ , $C_{d0,p}$ and Re_p defined by:

$$\chi = 3.7 - 0.65 \exp[-(1.5 - \log_{10} Re_p)^2 / 2] \quad (15)$$

$$C_{d0,p} = (0.63 + 4.8 / Re_p^{0.5})^2 \quad (16)$$

$$Re_p = \rho_f d_p \varepsilon_p |u_f - u_p| / \mu_f \quad (17)$$

u_p is particle velocity, $\varepsilon_p = 1 - \sum_{j=1}^n V_j / \Delta V$, d_p is particle diameter, $p = 1 \div n$.

The information is exchanged between the separate computations of the solid phase and of the fluid phase through the coupling term $\mathbf{f}_{p,f}$ of the particle–fluid interaction force. The DEM simulation provides the updated locations of each and every particle for the calculation of the volume fraction of fluid ε_f in each cell in Eq. (10). The CFD simulation provides the updated pressure field and velocity field for the calculation of the drag force, the pressure force and the viscous force acting on each particle that appear in both Eq. (1) and Eq. (10).

The viscous term is also included in DEM formulation. Model A is already implemented in CFDEM.²³ The so-called “non-resolved approach” presented here is applicable to those cases where particle sizes are smaller than the computational grid, thus the particles are assumed to not completely fill a computational cell. It is important when the flow Reynolds number is very low, which is the case for our study, especially when the fluid viscosity is relatively high and fluid velocity is low.

3. DEM simulations and results

The coupled CFD–DEM formulation in Section 2 was implemented as Model A in the CFDEM program. The CFDEM program is a highly parallelized computational platform that combines the LIGGGHTS program for the DEM modelling and the OpenFOAM program for the CFD modelling.²³ The numerical simulations in this study were executed on a High-Performance Computer System, which was equipped with 22 multi-threading processors Intel Xeon® E5-2699 Version 4 with a clock speed of 2.20 GHz and 500 GB of memory. A typical simulation could take more than a week to complete even with the parallel computation that utilized as many as 42 threads using the Message Passing Interface (MPI) protocol.

The simulations in this study were utilized to investigate the sand production behaviour of a weak sandstone as part of a larger project of both experimental and simulation studies in order to understand the significant sand production problem in certain shallow oil reservoirs in Kazakhstan. The simulations here aim to provide the additional microscopic information to the experimental investigations on a cylindrical sample,³⁸ which was prepared in the laboratory in the sequential steps of consolidation, cementation, perforation and sand production to mimic what had happened in the oil fields.

Similar to the procedure in the laboratory, a complete simulation is comprised of the following steps of the particle generation and pluvial deposition, consolidation, cementation, perforation and sand production.

3.1. Initial sample preparation

Numerical initial sample preparation process consists of three main stages: particle generation and pluvial deposition, consolidation, cementation.

The numerical particles were generated randomly inside a cylindrical wall and let fall under gravity to the bottom wall of the space to simulate a pluvial deposition process. The number and the size of the particles were specified such that they follow the particle size distribution of a real sandstone from the Ustyurt-Buzachi Sedimentary Basin.³⁹ A total of 10^5 frictional elastic auto-adhesive particles were generated to create the numerical sample, that is equivalent to a total mass of 1.57 g. A summary of the particle information is given in Table 1, while the numerical particle size distribution is compared to the real material in Fig. 3.

The micromechanical parameters for DEM simulations were adopted from the numerical studies of weak sandstones behaviour Rakhimzhanova et al. (2019) and are given in Table 2, the roles of the inputs are defined in the numerical formulations in Section 2.

To simulate the overburden stress in the field, the pluviated particles are compressed vertically by a top wall while they are surrounded and constrained by the cylindrical wall. This process simulates the one-dimensional compression condition of the consolidation of the reservoir’s material. The original JKR model were used to particle generation and pluvial deposition, consolidation processes so that particles were bonded, and a porous sample

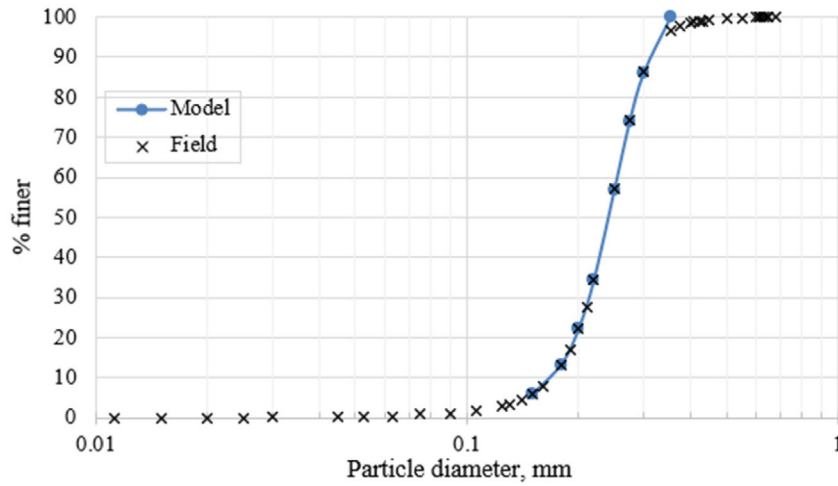


Fig. 3. Particle size distributions of the numerical sample and the real sandstone.

Table 1

A summary of the particle numbers and sizes in numerical simulation.

Particle diameter (mm)	0.15	0.18	0.2	0.22	0.25	0.275	0.3	0.355
Number of particles	20754	15525	13346	13821	17510	9922	5418	3704
Mass ratio (%)	5.8	7.5	8.8	12.16	22.64	17.05	12.1	13.95
Mass (milligram)	91.7	118.5	139.8	192.6	358.1	270.1	191.5	216.9

Table 2

Properties of the numerical particles.

Young's Modulus (Y , Pa)	$7 \cdot 10^{10}$
Poisson Ratio (ν)	0.3
Coefficient of Friction (μ_c)	0.3
Interface Energy (γ , J/m ²)	40
Particle Density (ρ_p , kg/m ³)	2500

could be prepared as in the field with an initial porosity of about 35%. Once the vertical stress was equal to the target value of 1 Mpa, the consolidation simulation is complete. The cementation of the numerical sample was activated as the contact model was switched from the original JKR model to the modified JKR model such that from this point onwards if new contacts are formed, they will be unbonded as specified by the Hertz's model. Bonds can break but no new bond can be created. As the modified JKR was activated, a certain number of bonds broke if the contact force condition had passed point C in Fig. 2. The numerical sample was allowed to reach new equilibrium and the sample preparation was considered complete. The intact sample after preparation is shown in Fig. 4a. The diameter (D) of the intact sample is equal to 15.12 mm, and the height (H) is equal to 6.471mm. The intact sample was then subjected to perforation and sand production that create damages to its initial structure and this process was captured in the microscopic simulation.

3.2. Sample perforation

The intact sample was perforated to create an escape path for the liquid flow as similar to the process in the oil well, which was simulated as the penetration of a penetrometer with an octagonal cross-section as shown in Fig. 4b. The dimensions of the penetrometer are given as $r = 0.7$ mm, $s = 0.579$ mm, $d_1 = 10$ mm, $d_2 = 1$ mm.

The cylindrical sample was divided into eleven annular cylinders of the same thickness as the radius (r) of the penetrometer such that we can monitor and characterize the internal structural evolution of these different zones as a function of the radial

distance from the centre of the sample. Note that the annular cylinders in Fig. 5 were only used for visualization and collecting data but it was not included in the computation.

The vertical penetrometer was driven along the axis of the cylindrical specimen. Although not shown in Fig. 6, the top wall used to compress the sample in previous step was fixed in-place to maintain the applied vertical stress and to prevent particles from escaping the specimen. This is similar to the experimental condition, where the perforation was created through a central opening in the top cap.³⁸ There was no interaction between the top wall and the penetrometer in the simulation. The sample was perforated to the full depth and then the penetrometer was extracted as shown in Fig. 6. The velocity of penetrometer in both stages was set as 12 m/s, when the time step of the DEM simulation was set at 7×10^{-10} s. We have selected the sizes of sample and penetrometer similar to those of Oryem et al. (2016) and O'Connor et al. (1997).^{40,41} The main criteria were the sample/penetrometer (equal 10.8) and penetrometer /particle ($3.94 \div 9.33$) ratios. Climent et al. (2014) used the averaging volumes to compute stresses and the width of the rings which were selected so that each ring contained enough number of particles that is statistically significant stress value as could be calculated. In this study the width of the rings (Fig. 5) is equal to penetrometer radius.

The colour of the particles in Fig. 6 was coded according to the average number of bonds in each annular cylinder. Here, the average bond number (N_b^i), the average contact number (N_c^i), and the average total contact number (N_t^i) in an i th annular cylinder can be calculated as:

$$N_b^i = \frac{\sum_{j=1}^{k_i} N_b^j}{k_i} \quad (18)$$

$$N_c^i = \frac{\sum_{j=1}^{k_i} N_c^j}{k_i} \quad (19)$$

$$N_t^i = N_b^i + N_c^i \quad (20)$$

where N_b^j and N_c^j are the number of bond and the number of contacts of a j th particle in the i th annular cylinder. The summation goes through the list of the total number of particles (k_i)

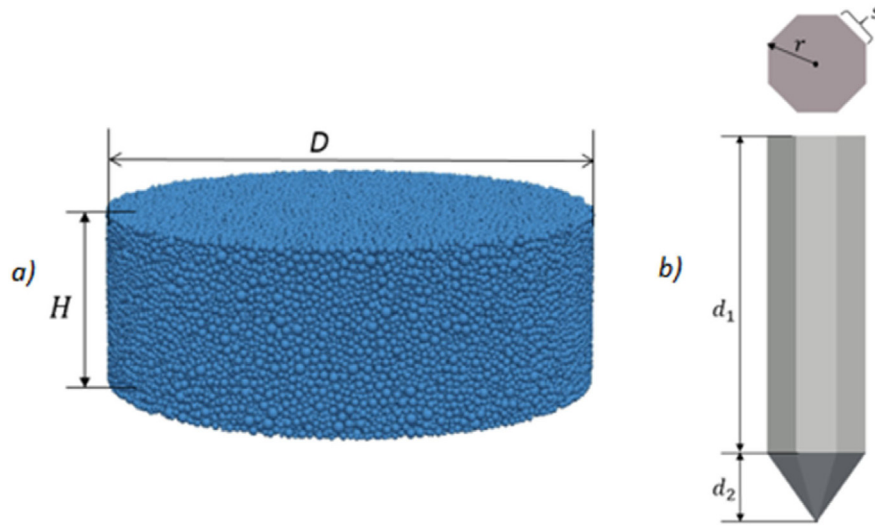


Fig. 4. (a) Initial sample before perforation when the vertical stress is equal to 1 MPa. (b) Penetrometer.

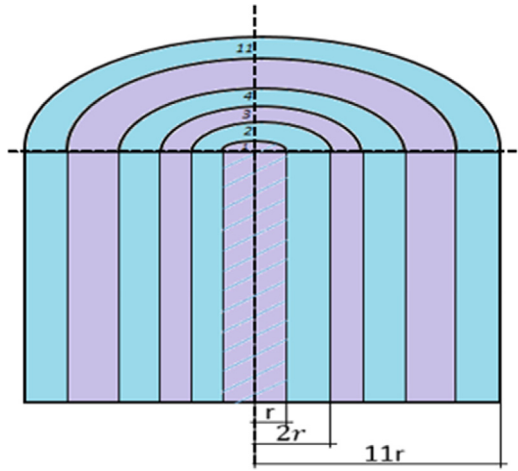


Fig. 5. Division of the cylindrical sample into annular cylinders for visualization and data collection.

in the i th cylinder, where $i = \overline{1 \div 11}$. Note that the modified *JKR* contacts were counted as bonds, all of which were formed before the perforation. The Hertz contacts that were formed only after the initial intact state were counted as contacts. A particle can have multiple contacts that include both bonded (N_b) and unbonded contacts (N_c).

The maximum bond number was observed in Fig. 6a at the beginning of the perforation, where the single red colour code indicates the homogeneity of the intact sample. As the penetration progressed, the number of bonds dropped quickly around the penetrometer, while the materials close to the boundary remained in its intact state in term of the maximum bond number. When the penetrometer was fully extracted as in Fig. 6e, a damage zone of approximately zero bonded particles was formed within a radial distance of $3r$ from the axis of the sample. A larger zone of up to about $7r$ was detected around the penetrometer where the particles in this zone lost certain bonds during the perforation process.

For better quantitative analysis of the bond breakage behaviour, the average number of bonds and the average number of contacts were plotted in Fig. 7 as a function of the radial distance from the axis of the numerical sample. The time given

in the legend were corresponding to the different stages of the perforation process in Fig. 6. Note that the green lines start at the distance $2r$, while the other curves start at the distance r . This is because the green lines correspond to the full penetration as in Fig. 6c, and there was no particle within the distance r this stage as it was occupied by the penetrometer.

The values of N_b and N_c are almost constant in the intact state, the small values of N_c were created between the two stages of consolidation and cementation when the modified *JKR* model was activated during the sample preparation process. N_b drops to values close to zero at $2r$ and is less than 1 at $3r$ at the end of perforation. N_c increases significantly in this zone when particles formed new contacts as they rearrange after the bonds were broken. The formation of new contacts is however less than the breakage of bonds and hence the total contact number N_t is less than the value in the intact state.

New contacts were not formed from the distance $7r$ outwards although the bond number drops about 10% (that is equivalent to a reduction of about 0.4 in magnitude) in this zone, which could mean that the bond breakage is not sufficient to trigger significant particle rearrangement to form new contacts. As bond breakage was not reversible, it represents plastic deformation. Particles, however, do not rearrange and the strain could be very small. One would argue that the materials between $7r$ and the boundary could be in the elastic (the term “elastic” is used in order to distinguish the plastic zone with the non-plastic one) state in a less stringent sense, and the distance $7r$ from the sample's centre can be considered as the interface between the plastic zone and the elastic zone that surround the perforation. The zone until $3r$, on the other hand, can be considered the zone of perforation damage, where the interparticle bonds were mostly destroyed leading to significant particle rearrangement.

The sample was created with particles of eight different sizes. The bond number N_b was counted separately for each particle size (see Table 1). In general, the larger particles developed more contact and bond with other neighbouring particles as compared to the smaller particles, but it is not yet known which particle size is more prone to bond breakage. This information would be useful in the later stage of sand production as the unbonded particles could be eroded more easily by the hydrodynamical forces from the fluid flow. The change in the N_b number can be calculated as:

$$\Delta N_b(\%) = \left(\frac{(N_b)_t - (N_b)_{t0}}{(N_b)_{t0}} \right) * 100\% \quad (21)$$

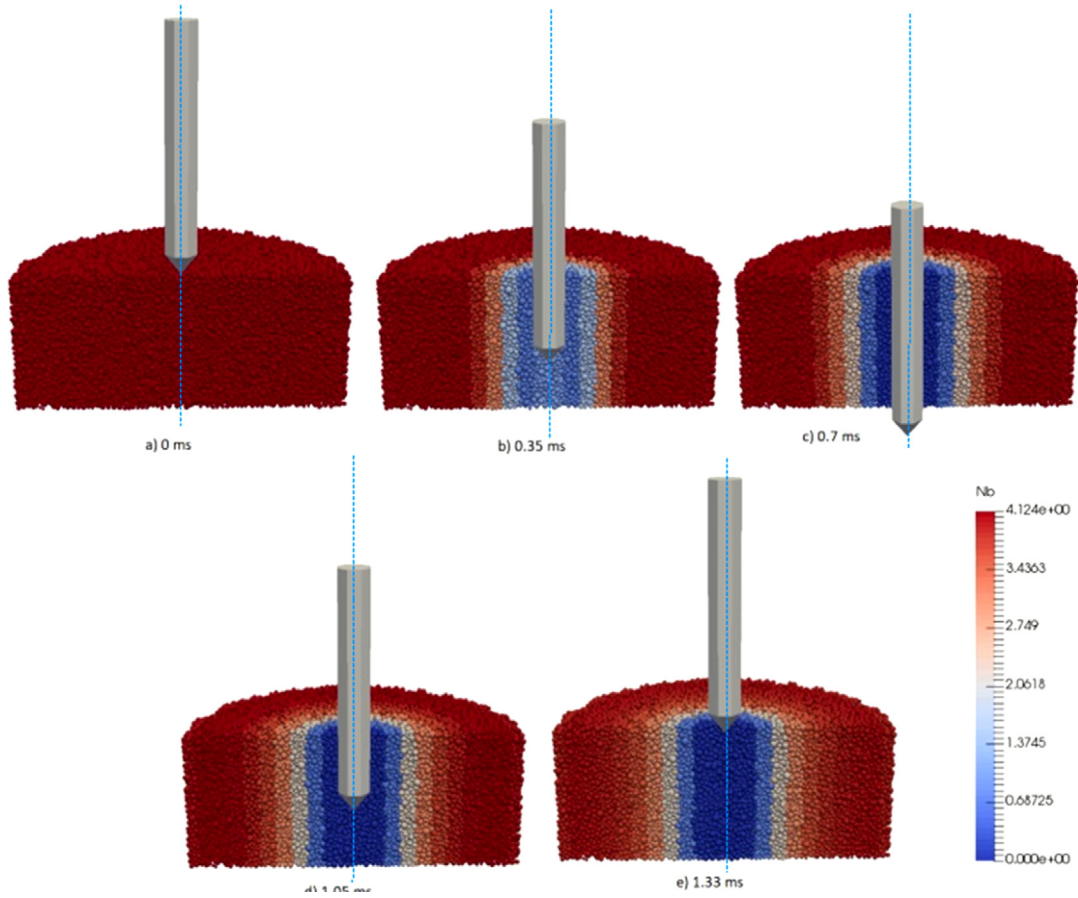


Fig. 6. 3D Perforation simulation test. Particles are coloured according to the bond number N_b .

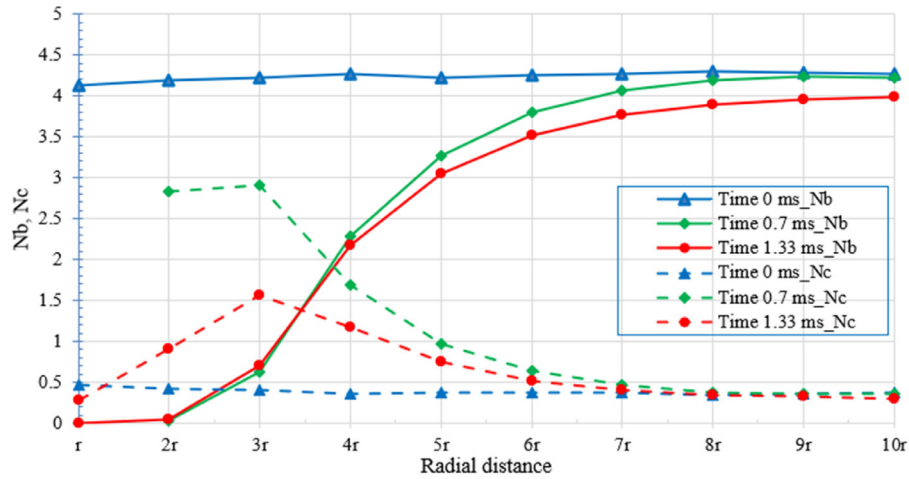


Fig. 7. Perforation test. The behaviour of average bond and contact numbers (N_b , N_c) vs distance from the centre of sample.

where $(N_b)_t$ is the N_b value at time t ; t -current time; and t_0 - the time at the beginning of the perforation process in Fig. 6a. The results of N_b and ΔN_b were calculated for the three steps of Fig. 6a, 6c and 6e and presented in Table 3. In the initial state, the largest particle size has in average 7.65 bonds, which is more than double the number of the smallest particle size (~ 3.14). At the end of perforation (Fig. 6e), each particle size lost 17% to 20% of its bonds, a majority of which occurred between the initial state and the full penetration state in Fig. 6c. There is no distinctive difference in the bond breakage behaviour among different particle sizes. The largest particles still have more than

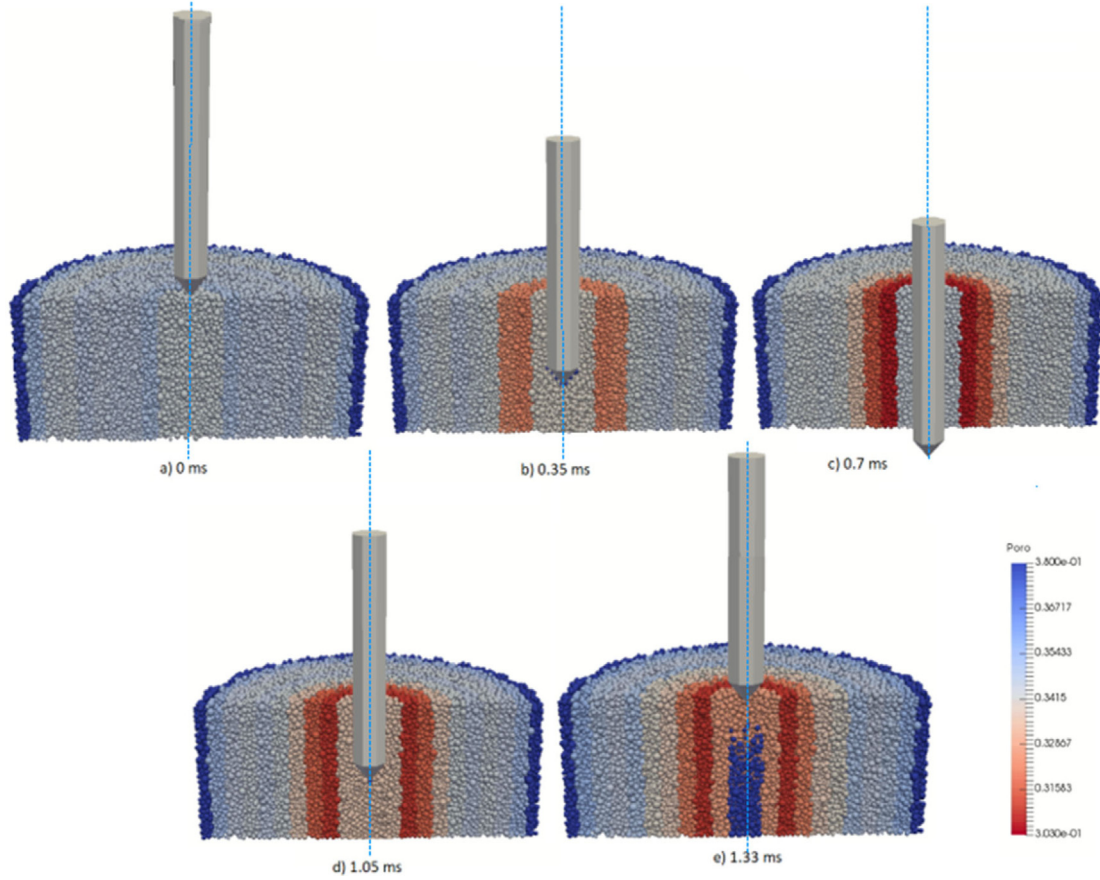
double the number of bonds than the smallest particles at the end of perforation.

The permeability of the material is directly related to the porosity. The permeability of the plastic zone is an input that was found having significant impact on the prediction of sand production using analytical model.⁴² The porosity was calculated for the annular cylinders in Fig. 5. First, the volume of all particles, V_p^i , located within each annular cylinder can be determined as:

$$V_p^i = \sum_{j=1}^{m_i} V_j \quad (22)$$

Table 3Bond number (N_b) and the change of bond number (ΔN_b) for different particle sizes.

Time step	Diameter (mm)	0.15	0.18	0.2	0.22	0.25	0.275	0.3	0.355
0 ms	N_b	3.14	3.50	3.78	4.13	4.76	5.35	6.03	7.65
	ΔN_b (%)	0.00	0.00	0.00	0.00	0.00	0.00	0.00	0.00
0.7 ms	N_b	2.72	3.01	3.25	3.55	4.09	4.61	5.22	6.70
	ΔN_b (%)	-13.25	-13.78	-14.12	-14.10	-14.06	-13.84	-13.53	-12.45
1.33 ms	N_b	2.59	2.84	3.04	3.31	3.81	4.28	4.81	6.19
	ΔN_b (%)	-17.38	-18.74	-19.65	-19.83	-20.06	-20.11	-20.22	-19.08

**Fig. 8.** Internal porosity distribution during perforation, the colour codes indicate the porosity values.

where V_j is the volume of the individual particle; m_i -total number of particles in the i th cylinder, $i = 1 \div 11$. The porosity of the i th cylinder (ϕ_i) can be determined as:

$$\phi_i = \frac{V_i - V_p^i}{V_i} \quad (23)$$

where V_i is the volume of the i th annular cylinder, which is the same for all cylindrical regions.

As the penetrometer was driven into the sample, particles in the surrounding were pushed out radially. A compacted zone was formed within the distances $2r$ to $6r$. When the penetrometer was extracted these zones expanded slightly that is reflected in the lighter reddish colours. The most compacted zone of the reduced porosity was between $2r$ to $3r$, whereas a loose zone of unbonded particles was formed in the lower half of the cavity left by the penetrometer. Note that in the zone of less than $3r$ radial distance, most of the bonds have been broken (see Fig. 7). The significant change in the porosity value describes particle rearrangement and large deformation, which agree with the results of bond breakage in the previous part. The zone from $6r$ to the boundary did not show any noticeable change in the

porosity. The outmost annular ring showed an anomaly due to the effect of the boundary condition (see Fig. 8).

The radial distributions of the porosity during perforation were given in Fig. 9. Similar to Fig. 7, the green line representing the full penetration state is started at the distance $2r$ as the space below r was occupied by the penetrometer. The porosity distributions from $6r$ outwards do not show any significant change during the whole perforation process. If porosity change is considered as the criteria that differentiates the plastic zone and the elastic zone, the interface between them can be considered as $6r$ in Fig. 9, which is smaller than the interface at $7r$ in Fig. 7. The small variations in the bond number and the contact number in Fig. 7 were not translated to a noticeable change in the porosity. The largest reduction of porosity was obtained at $3r$, the same distance of the maximum particle rearrangement in Fig. 7. The porosity of the loose material inside the cavity after perforation was obtained as 65%, while the porosity in the elastic zone remains the same as the intact porosity. A more quantitative analysis of the change in porosity is given in Table 4, the values in which were calculated similar to Eq. (21). It is confirmed that the maximum porosity reduction in the surrounding regions of the

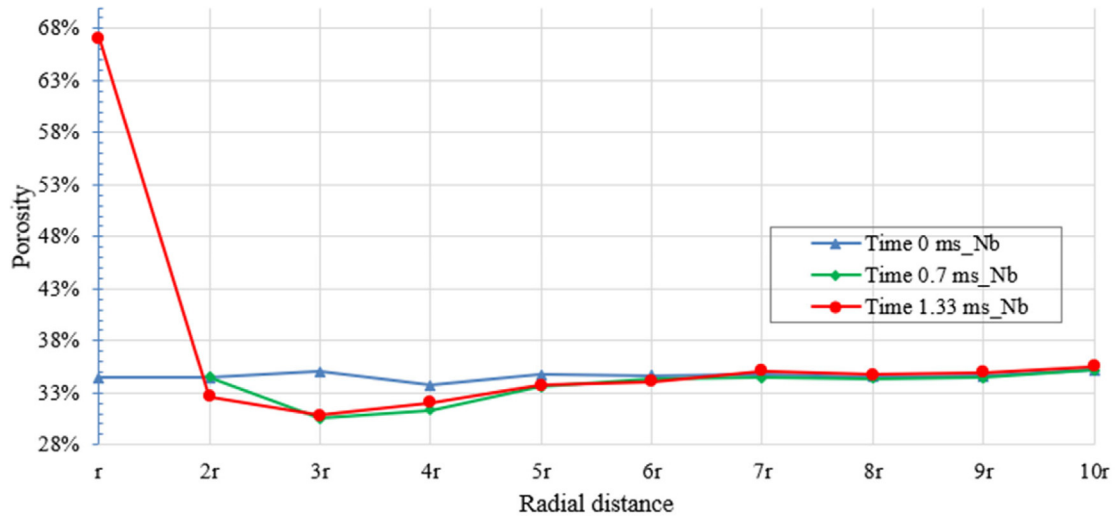


Fig. 9. Distribution of porosity along radial distance during perforation.

Table 4
Change in the porosity value during perforation.

Time step	Radial distance	r	$2r$	$3r$	$4r$	$5r$	$6r$	$7r$	$8r$	$9r$	$10r$
0.7 ms	$\Delta\phi_i$ (%)		0.2	-12.9	-7.1	-3.3	-1.1	-1.0	-0.4	-0.5	0.0
1.33 ms	$\Delta\phi_i$ (%)	94.8	-5.2	-12.0	-5.0	-2.9	-1.8	0.7	0.6	0.9	1.0

penetrometer occurred at $3r$. During the extraction of the penetrometer, the materials in the zone until $2r$ expand significantly, while it is much less significant for the zone from $3r$ outwards. The creation of a zone of lower permeability at $3r$ would affect the fluid flow in the sand production stage. The change of the porosity in the zone between $6r$ and $10r$ can be considered negligible.

The poroelastoplasticity analysis of stresses around a cylindrical cavity assumed that the material behaves elastically until the effective stresses fulfil the failure criterion. As the material behaviour changes from elastic to plastic, a plastic zone is created around the cavity. The plastic zone properties such as porosity, permeability, may significantly different from the elastic zone properties.^{43,44} The numerical simulation results were used to confirm the formation of the plastic zone where the regions with the broken bonds were considered as the plastic zone.²⁹ The porosity values of the plastic zones were converted into permeabilities and compared to the permeability from the semi-analytical results based on the experimental data.²⁹ It was shown that the permeability reduction patterns were similar in both numerical and experimental studies (Fig. 10). Normalization was adopted to qualitatively compare the data trend across different boundary conditions between two studies.

4. Coupled simulations and sand production results

The loading conditions in the simulations were made comparable to the experimental studies of the same sandstone material in the laboratory,²⁸ which was conducted using a newly developed High Pressure Consolidation System (HPCS). The experimental system is equipped with a Servo-hydraulic Compression Load Frame of 5000 kN capacity, which allows the vertical compression and in-situ cementation of a cylindrical specimen of 300 mm diameter inside a rigid cylinder (i.e. one dimensional compression). Fluid was then injected into the cemented sample from the outer boundary of the cylindrical mould under the conditions of up to 7 MPa maximum fluid pressure and up to 5 l/min flow rate. The outflow is directed to a fluid collection system and a solid separation system such that the produced sand can be

measured during the sand production process. The schematic and the general view of the apparatus are given in Fig. 11, whereas further details can be found in the report of the experimental results.²⁸ The vertical compression, in-situ cementation and sand production processes in the experiment are closely simulated in this numerical simulation. Their applicable results are compared in this study.

4.1. Coupled simulations

The perforated sample in previous simulation was used for sand production simulation where water was injected radially from the external boundary towards the vertical perforation tunnel at the centre as similar to the experimental conditions. The sand production simulation was conducted using the CFDEM coupling open-source program.²³ Water was considered incompressible with the density $\rho_w = 1000 \text{ kg/m}^3$ and the kinematic viscosity $\mu_w = 10^{-6} \text{ m}^2/\text{s}$. The CFD computational domain in Fig. 12 has 3920 cells that form a cylinder of the same size as the initial sample in Fig. 4a. The boundary conditions are illustrated in Fig. 12. The top and the bottom walls were set as impermeable walls with no-slip boundary condition. There was a central opening on the top wall to serve as the fluid outlet. Water was injected from the whole circumferential wall of the cylinder at a constant velocity $v = 10^{-5} \text{ m/s}$. The outlet pressure was maintained at a constant $P = 1 \text{ MPa}$.

The interactions between the fluid and the particle phases were simulated by a two-way coupling method.⁸ The motion of particles affects the motion of fluid and vice versa. The coupling information was given in terms of the pressure force, the viscous force and the Di Felice drag force^{36,37} as they were explained in Eq. (1) and Eq. (10). The total solid mass, M_t , of 10^5 particles was 1.57 g. The critical DEM time-step Rayleigh time is based on the average particle size and a fraction of this is given by the following equation⁴⁵:

$$dt_r = \pi \cdot r_{min} \cdot \sqrt{\frac{\rho_p}{G}} / (0.1631 \cdot v + 0.8766) \quad (24)$$

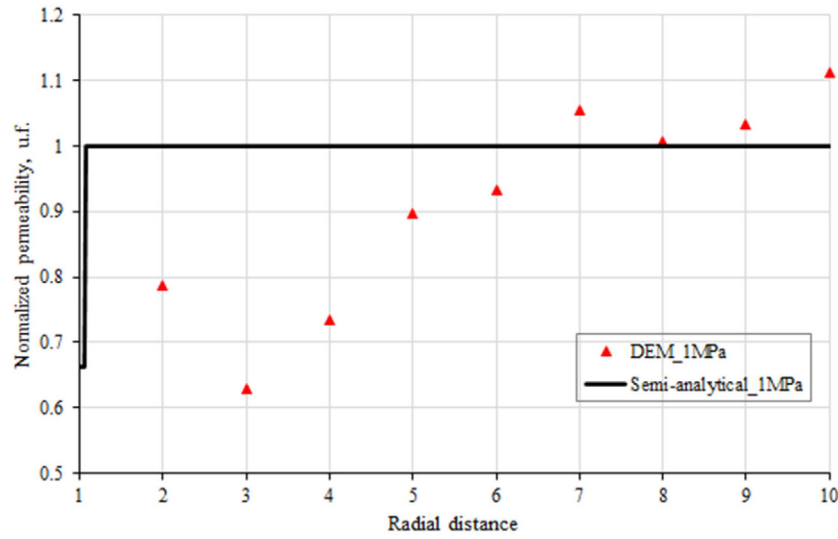


Fig. 10. Normalized permeability from numerical simulation and semi-analytical study.²⁹

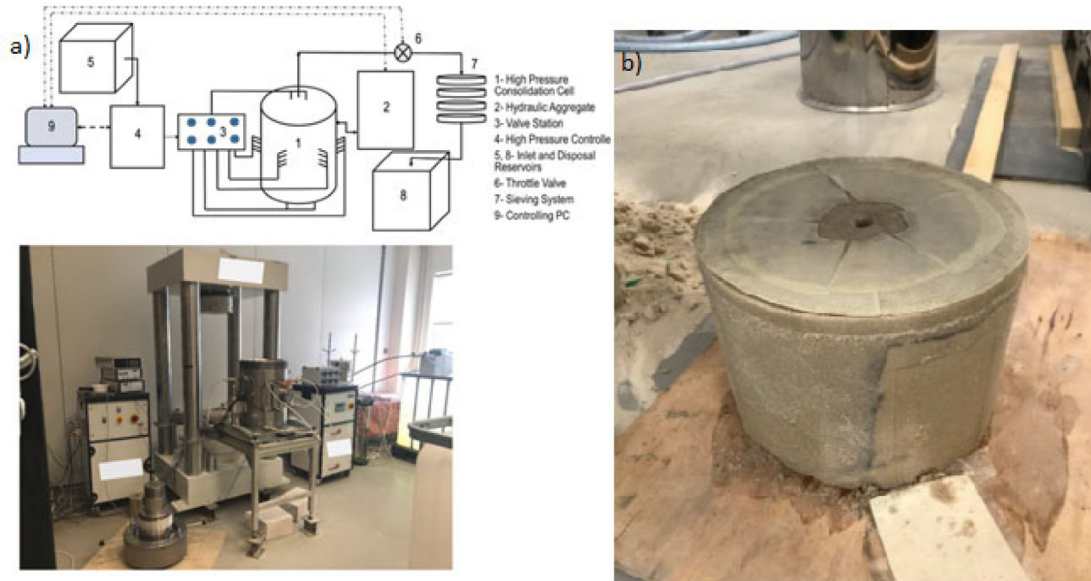


Fig. 11. (a) General View of High Pressure Consolidation System and (b) Perforated specimen retrieved after the sand production tests.³⁸

where G is particle shear modulus, r_{min} -is minimal radii of particles in sample.

The DEM time step is $1.0e^{-8}$ that is 5.18% from Rayleigh time $dt_r = 1.93e^{-7}$. The CFD time is $1.0e^{-6}$ under which a maximum Courant number of 0.0167. Similar to Goniva et al. (2012) the time-step size for the CFD solver have been chosen in a way that it is an integer multiple of the DEM time-step. This is to save computational time, i.e. the CFD simulation was run for every **100** time steps of the DEM simulation and the coupling data was exchanged accordingly. Influence of coupling frequency on CFD-DEM result was not considered in this study.

The coupled simulation was run for more than 10 milliseconds, during which there were a total of 19 particles that were produced together with the outflow of water from the sample. The discrete events of sand production and the cumulative sand mass were given in Fig. 13. There was no sand produced after 7.5 ms and the total produced sand mass was about 0.23 mg, which is 1.47% of the total mass M_t . The sand production behaviour can be characterized as a two-stages process, where the sanding events

were more frequent in the first stage when time was less than around 2.5 ms. In the second stage between 2 ms and 8 ms, the sanding events were less frequent, and they were associated with the production of bigger particles that are presented by the higher bars and the larger sand masses in Fig. 13. In general, the sanding phenomenon decreased over time, which indicates a transient sand production.⁴

The sand production results in Fig. 13 can be separated into the production of different particle sizes in Fig. 14. The results were plotted for two different time intervals of approximately the first stage of a frequent sand production and the second stage of a fewer sand production events based on the results in Fig. 13. It is clear that the five smaller particles were produced first, while the sixth and the seventh largest particles were only produced in the second stage and none of the eighth largest particles was produced during the whole sand production simulation.

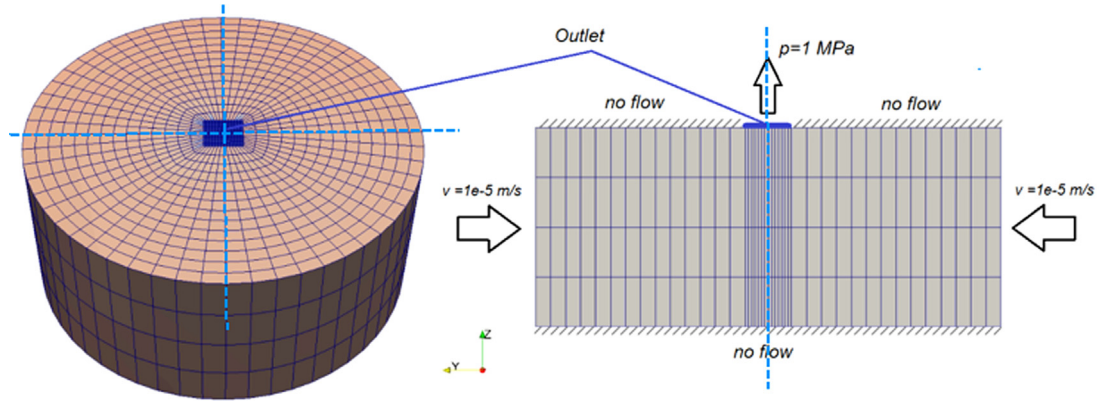


Fig. 12. CFD simulation domain and boundary conditions.

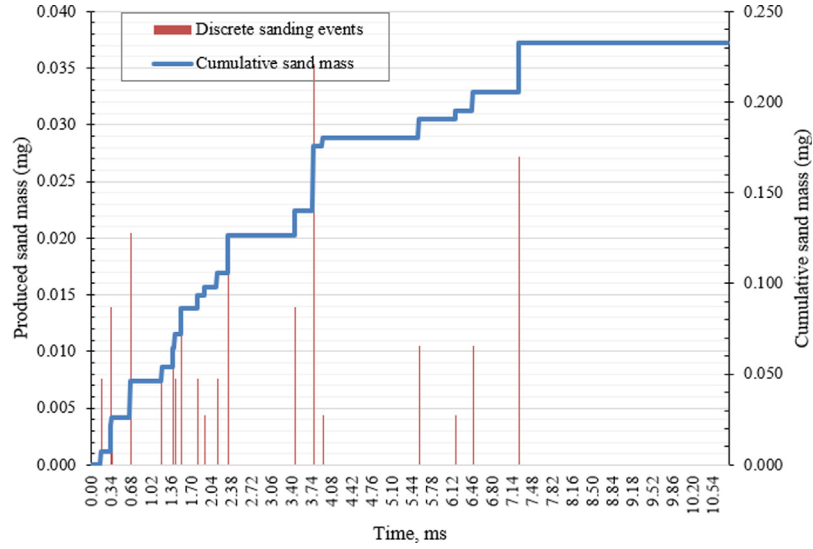


Fig. 13. Sand production results.

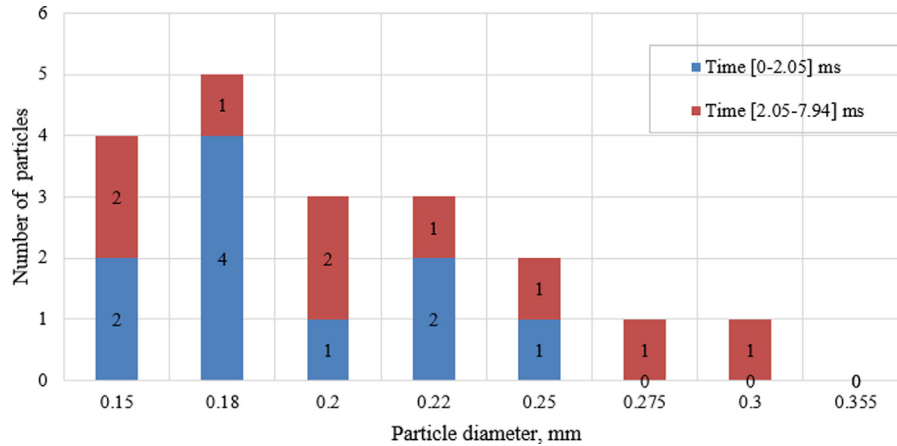


Fig. 14. The number of produced particles depend on particle sizes.

4.2. Microscopic analysis of the sand production results

The results of the CFD simulation and of the DEM simulations are compared side-by-side in terms of the fluid velocity and the particle velocity in Fig. 16. There was a large mobilization of the particles near the outlet in the beginning of the sand production simulation that was associated with a distribution

of high fluid velocity in Fig. 16a. The rapid fluid flow moving out of the specimen forced the particles towards the exit, which triggered more particle productions in the beginning as shown in Fig. 13. The dynamic zones of the particle and the fluid movements decrease in size in Fig. 16b and Fig. 16c, which reflects a stabilization mechanism in the granular structure of the sample as the majority of particle movements had ceased. This could

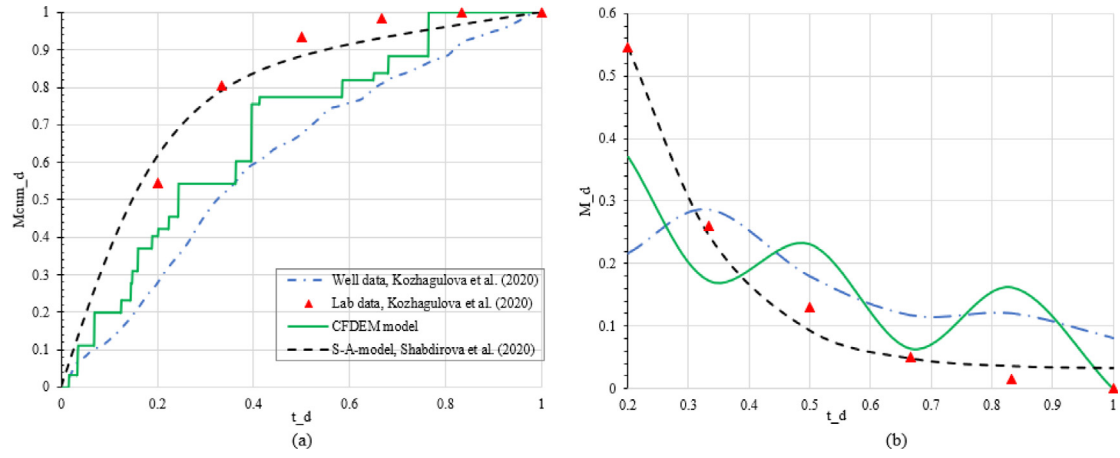


Fig. 15. Comparison of the simulation results with laboratory and well data. (a) cumulative sand production (b) sand production increment.

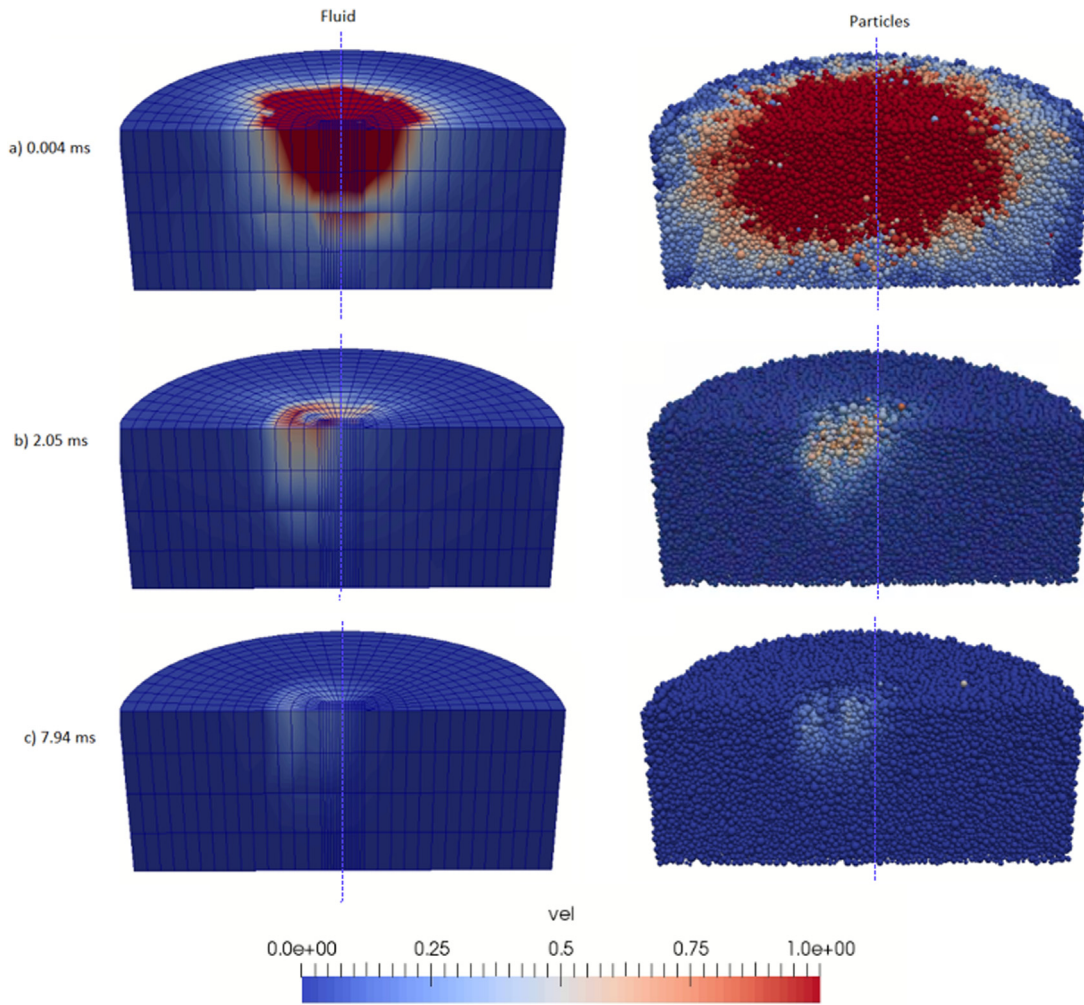


Fig. 16. 3D Sand production simulation. Flow and particles velocities (in m/s) at different time steps.

be due to the sand arching mechanism, which was described in the studies of sand production both in the well,^{46,47} and in the laboratory.^{48,49} The velocity distributions inside the sample became nearly homogeneous in Fig. 16c, when there was no longer sand production (see Fig. 13). The fluid flow became steady state as the sand production ceased. This agrees with the transient sand production behaviour observed in the experimental study by Kozhagulova et al. (2020), where a steady state fluid flow was

obtained for a constant pressure draw down after and a sand production in the beginning.

In order to compare simulation results with laboratory and well data which are in different time and geometric scale, normalization of the data was adopted to provide dimensionless parameters for the comparison. The dimensionless time interval

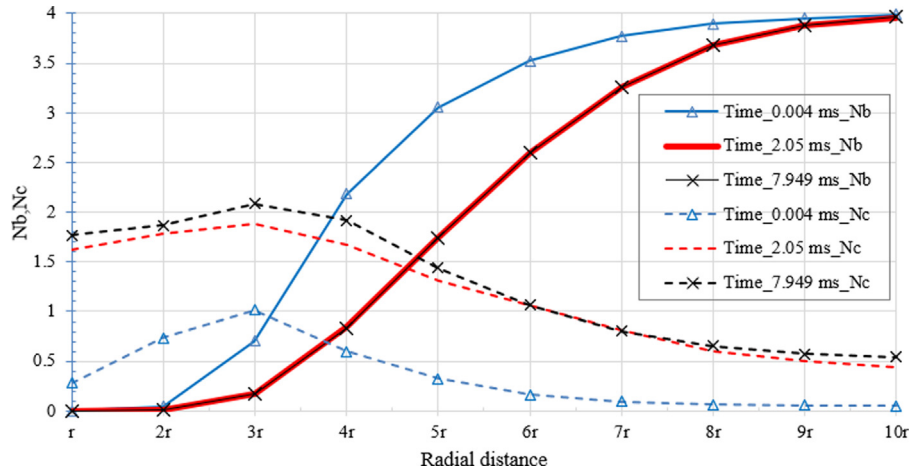


Fig. 17. Sand production. The behaviour of average bond and contact numbers (N_b, N_c) vs distance from the centre of sample.

Table 5
Number of particles (m_i) in the annular cylinders, $i = \overline{1 \div 10}$.

Time step	Radial distance	r	$2r$	$3r$	$4r$	$5r$	$6r$	$7r$	$8r$	$9r$	$10r$
0.004 ms	m_i	474	2657	4659	6225	7923	9746	11289	12920	14686	16271
2.05 ms	m_i	808	2406	4190	6031	7969	9788	11444	13004	14786	16355
7.94 ms	m_i	799	2397	4204	6039	7954	9769	11467	13004	14791	16359

is defined as follows:

$$t_d = \left(\frac{t}{t_{end}} \right) \quad (25)$$

where t - current time; and t_{end} - the time period up to the moment when sand production ends in produced liquid. The dimensionless time intervals vary between 0 and 1, where 0 corresponds to the start of production and 1 corresponds to the time at the end of sand production t_{end} .

The dimensionless cumulative sand production is given as:

$$Mcum_d^t = \left(\frac{\int_{t=0}^t M_t dt}{\int_{t=0}^{t_{end}} M_t dt} \right) \quad (26)$$

where M_t - is the instantaneous sand rate and ∇t is the time interval.

The sand production increments that reflect different sanding rates at different time intervals were calculated as:

$$M_d^i = (Mcum_d^i - Mcum_d^{i-1}) \quad (27)$$

where $i \in t_d$.

The simulation results were compared with the laboratory data and well data²⁸ and the data of a semi-analytical model for sand erosion prediction⁵⁰ in Fig. 15. Despite the wide ranges of the overburden stress, drawdown pressure, and geometrical scale among different studies, the qualitative comparisons in Fig. 15 show a similar pattern of decreasing sand production increments from an initial maximum sand rate of a transient sand production for the different boundary conditions. Further quantitative analysis between different data sets will be considered in future works.

Fig. 17 shows the bond number and the contact number values during sand production, which were calculated using Eqs. (18) and (19); the time steps in the legend are corresponding to Fig. 16. The major changes in the bond number and the contact number happened between the two states in Figs. 16a and 16b, while a much smaller change happened in the second stage of a few sand bursts as described in Fig. 13. The contact number increased across the sample's radius in Fig. 17, which agrees with the results in Fig. 16a that showed the majority of the sample's

particles were moving with high velocities. This indicates that the plastic zone's boundary at $7r$ defined in term of the particle rearrangement in Fig. 7 had grown to occupy the whole sample under the fluid flow condition of the sand production process. The growth of the contact number near the perforation in Fig. 17 would facilitate an increase of the frictional resistance at the new contacts that could give rise to the formation of a sand arch around the orifice. Note that the distance $3r$ was the location of the greatest contact number, which had been defined previously as the boundary of the perforation damage zone.

The numbers of particles located in each annular cylinder are given in Table 5, while the percentage of change of these values is given in Table 6. During the sand production simulation, particles migrated from the zones between $2r$ and $4r$ to the central perforation tunnel (within r). The numbers of particles dropped 10% in the zones $2r$ and $3r$, while it increased as much as 70% in the perforation tunnel. Particles in the zones from $5r$ outwards did not migrate as much because they were still bonded by a larger bond number than the contact number (i.e. $N_b > N_c$). The produced particles are only a small fraction of the total particles and they would be among the unbonded particles that migrated from the perforation damage zone.

The results of the porosity change during sand production are given in Fig. 18 and Table 7. As more particles migrated to the perforation tunnel, the porosity in this zone dropped quickly from 65% to 40%. The porosity in the zones between $2r$ and $4r$, on the other hand, increased as they lost particles. Note that these are the compacted zones of lower porosity that were created during the perforation process, and here they expanded the most under the fluid flow condition. Although the plastic zone in terms of bond breakage and new contact formation had grown to occupy the whole sample (see Fig. 17), the smaller perforation damage zone played a more important role in the production of sand particles. It represented the clusters of the unbonded particles in a compressed state; when subjected to fluid flow, it rebounded easily and released its particles to attain a looser state of higher porosity.

The porosity inside the sample at the end of the transient sand production is mostly greater than the intact porosity value of 35%.

Table 6
Change of particle numbers in the annular cylinders.

Time step	Radial distance	r	$2r$	$3r$	$4r$	$5r$	$6r$	$7r$	$8r$	$9r$	$10r$
0.004 ms	$\Delta m_i(\%)$	0.0	0.0	0.0	0.0	0.0	0.0	0.0	0.0	0.0	0.0
2.05 ms	$\Delta m_i(\%)$	70.5	-9.4	-10.1	-3.1	0.6	0.4	1.4	0.7	0.7	0.5
7.94 ms	$\Delta m_i(\%)$	68.6	-9.8	-9.8	-3.0	0.4	0.2	1.6	0.7	0.7	0.5

Table 7
Change in the porosity value during sand production.

Time step	Radial distance	r	$2r$	$3r$	$4r$	$5r$	$6r$	$7r$	$8r$	$9r$	$10r$
0.004 ms	$\Delta \phi_i(\%)$	-2.46	0.30	-0.28	0.29	-0.06	0.05	0.04	-0.03	0.08	0.07
2.05 ms	$\Delta \phi_i(\%)$	-41.01	19.59	21.51	7.60	-1.50	-0.49	-2.57	-1.14	-1.30	-0.71
7.94 ms	$\Delta \phi_i(\%)$	-40.88	20.31	20.02	8.47	-1.21	-0.26	-2.98	-1.09	-1.33	-0.78

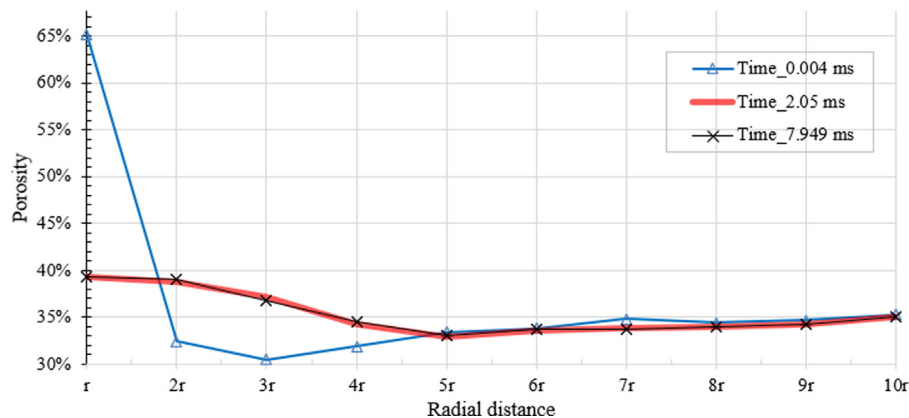


Fig. 18. Distribution of porosity along radial distance during sand production.

The perforation hence created a more favourable condition for the outflow of fluid from the sample as similar to the design purpose in the oil-gas industries.

5. Conclusions

A modified JRK model²⁴ has been implemented successfully in the open-source programs LIGGGHTS and CFDEM^{23,25} to simulate the bonding behaviour of a weak cemented sandstone in Kazakhstan. A numerical sandstone sample was prepared, perforated and subjected to radial fluid flow from the boundary in a series of different simulation stages. The number of bonded contacts and unbonded contacts were counted in every time step that allowed the estimation of the perforation damage, and of the plastic zone throughout the whole simulation process. Furthermore, the cylindrical sample was divided into eleven annular cylindrical zones around the central perforation tunnel and the porosity was calculated for each zone, which provided the internal porosity distribution across the sample. The perforation process was found to create a damage zone of about $3r$ to $4r$ thickness of the unbonded particles with nearly complete bond breakage in this zone, where r is the radius of the perforation tunnel. A compacted zone of lower porosity was embedded inside the perforation damage zone and under fluid flow condition, it expanded quickly to attain a porosity that is greater than the intact porosity as the particles of which migrated towards the perforation tunnel during sand production. The simulation described a transient sand production phenomenon, when small particles were produced first in a series of rapid events and followed by the production of larger particles in less frequent sand bursts. Particle movements inside the sample ceased once there was no longer sand production.

CRediT authorship contribution statement

Furkhat Khamitov: Methodology, Software, Formal analysis, Writing - original draft, Writing - review & editing, Validation. **Nguyen Hop Minh:** Conceptualization, Supervision, Writing - review & editing. **Yong Zhao:** Conceptualization, Supervision, Writing - review & editing.

Declaration of competing interest

The authors declare that they have no known competing financial interests or personal relationships that could have appeared to influence the work reported in this paper.

Acknowledgements

This research was sponsored by Nazarbayev University, Kazakhstan research grant. First author also would like to acknowledge the research grant, No AP08052762, from the Ministry of Education and Science of the Republic of Kazakhstan.

References

1. Acock A, O'Rourke A, Shirmboh D, et al. Practical approaches to sand management. *Oil F Rev.* 2004;16:10–27. http://www.slb.com/~media/Files/resources/oilfield_review/ors04/spr04/02_sand_management.pdf.
2. B. Dusseault M, El-Sayed S. CHOP - Cold heavy oil production. In: *IOR 1999-10th European Symposium on Improved Oil Recovery*. Brighton: European Association of Geoscientists & Engineers; 1999. <http://dx.doi.org/10.3997/2214-4609.201406351>.
3. Tremblay B, Sedgwick G, Forshner K. Modelling of sand production from wells on primary recovery. In: *Annual Technical Meeting*. Petroleum Society of Canada; 1996. <http://dx.doi.org/10.2118/96-26>.

4. Veeken CAM, Davies DR, Kenter CJ, Kooijman AP. Sand production prediction review. Developing an integrated approach. *Proc - SPE Annu Tech Conf Exhib.* 1991;Pt(1):335–346. <http://dx.doi.org/10.2523/22792-MS>.
5. Asadi M, Preston FW, Green DW, Ghalambor A. Effect of the perforation damage on well productivity. In: *SPE Formation Damage Control Symposium*, vol. 26. Society of Petroleum Engineers; 1994:1303–1314. <http://dx.doi.org/10.2118/27384-MS>.
6. Han G, Dusseault MB. Description of fluid flow around a well-bore with stress-dependent porosity and permeability. *J Pet Sci Eng.* 2003;40(1–2):1–16. [http://dx.doi.org/10.1016/S0920-4105\(03\)00047-0](http://dx.doi.org/10.1016/S0920-4105(03)00047-0).
7. Sinder PM, Benzal WM, Barker JM, Leidel DJ. Perforation damage studies in unconsolidated sands: Part II - Baseline studies and comparison of analytical methods for quantifying damage. *SPE Reserv Eng (Society Pet Eng).* 2000;(A):453–465. <http://dx.doi.org/10.2523/63117-MS>.
8. Rahmati H, Jafarpour M, Azadabakt S, et al. Review of sand production prediction models. *J Pet Eng.* 2013;2013:1–16. <http://dx.doi.org/10.1155/2013/864981>.
9. Fama MED. *Numerical Modeling of Yield Zones in Weak Rock*. Pergamon Press Ltd; 1993. [http://dx.doi.org/10.1016/0148-9062\(94\)90569-x](http://dx.doi.org/10.1016/0148-9062(94)90569-x).
10. Karmakar S, Sharma J, Kushwaha RL. Critical state elasto-plastic constitutive models for soil failure in tillage - A review. *Can Biosyst Eng / Le Genie des Biosyst au Canada.* 2004;46(Wood 1990):19–23.
11. Jing L, Stephansson O. Case studies of discrete element method applications in geology, geophysics and rock engineering. In: *Engineering*. 2007:447–538. [http://dx.doi.org/10.1016/S0165-1250\(07\)85012-7](http://dx.doi.org/10.1016/S0165-1250(07)85012-7).
12. Cundall PA, Strack ODL. A discrete numerical model for granular assemblies. *Géotechnique.* 1979;29(1):47–65. <http://dx.doi.org/10.1680/geot.1979.29.1.47>.
13. Tsuji Y, Kawaguchi T, Tanaka T. Discrete particle simulation of two-dimensional fluidized bed. *Powder Technol.* 1993;77(1):79–87. [http://dx.doi.org/10.1016/0032-5910\(93\)85010-7](http://dx.doi.org/10.1016/0032-5910(93)85010-7).
14. Narsilio GA, Buzzi O, Fityus S, Yun TS, Smith DW. Upscaling of Navier–Stokes equations in porous media: Theoretical, numerical and experimental approach. *Comput Geotech.* 2009;36(7):1200–1206. <http://dx.doi.org/10.1016/j.compgeo.2009.05.006>.
15. Irmay S. On the theoretical derivation of Darcy and forchheimer formulas. *Eos, Trans Am Geophys Union.* 1958;39(4):702–707. <http://dx.doi.org/10.1029/TR039i004p00702>.
16. Cheung LYG. Micromechanics of sand production in oil wells. 2010 <https://ethos.bl.uk/OrderDetails.do?uin=uk.bl.ethos.528300>.
17. Zhou ZY, Yu AB, Choi SK. Numerical simulation of the liquid-induced erosion in a weakly bonded sand assembly. *Powder Technol.* 2011;211(2–3):237–249. <http://dx.doi.org/10.1016/j.powtec.2011.04.029>.
18. Climent N. A coupled CFD-DEM model for sand production in oil wells. 2016 <http://hdl.handle.net/2117/105810>.
19. Potyondy DO, Cundall PA. A bonded-particle model for rock. *Int J Rock Mech Min Sci.* 2004;41(8 SPEC.ISS.):1329–1364. <http://dx.doi.org/10.1016/j.ijrmms.2004.09.011>.
20. Kenneth Langstreth Johnson KK, ADR. Surface energy and the contact of elastic solids. *Proc R Soc London A Math Phys Sci.* 1971;324(1558):301–313. <http://dx.doi.org/10.1098/rspa.1971.0141>.
21. Rakhimzhanova A, Thornton C, Amanbek Y, Zhao Y. Numerical simulations of cone penetration tests in cemented sandstone. 2019:1–15. <http://dx.doi.org/10.31224/osf.io/uhy36>.
22. Rakhimzhanova AK, Thornton C, Amanbek Y, Zhao Y. *Numerical Simulations of Sand Production in Oil Wells using the CFD-DEM-IBM Approach*. 2020:1–24. <http://dx.doi.org/10.31224/osf.io/pkteu>.
23. Goniva C, Kloss C, Deen NG, Kuipers JAM, Pirkers S. Influence of rolling friction on single spout fluidized bed simulation. *Particulology.* 2012;10(5):582–591. <http://dx.doi.org/10.1016/j.partic.2012.05.002>.
24. Rakhimzhanova AK, Khamitov FA, Minh NH, Thornton C. D DEM simulations of triaxial compression tests of cemented sandstone. In: *Proc IS Atlanta 2018 Symp Geomech from Micro to Macro Res Pract*; 2018.
25. Kloss C, Goniva C, Hager A, Amberger S, Pirkers S. Models, algorithms and validation for opensource DEM and CFD-DEM. *Prog Comput Fluid Dyn An Int J.* 2012;12(2/3):140. <http://dx.doi.org/10.1504/PCFD.2012.047457>.
26. Chen G, Xiong Q, Morris PJ, Paterson EC, Sergeev A, Wang Y-C. OpenFOAM for computational fluid dynamics. *Notices Amer Math Soc.* 2014;61(4):354. <http://dx.doi.org/10.1090/noti1095>.
27. Climent N, Arroyo M, O'Sullivan C, Gens A. Sand production simulation coupling DEM with CFD. *Eur J Environ Civ Eng.* 2014;18(9):983–1008. <http://dx.doi.org/10.1080/19648189.2014.920280>.
28. Kozhagulova A, Minh NH, Zhao Y, Fok SC. Experimental and analytical investigation of sand production in weak formations for multiple well shut-ins. *J Pet Sci Eng.* 2020;195(2019):107628. <http://dx.doi.org/10.1016/j.petrol.2020.107628>.
29. Shabdirova AD, Khamitov F, Kozhagulova AA, Amanbek Y, Minh NH, Zhao Y. Experimental and numerical investigation of the plastic zone permeability. In: *Am Rock Mech Assoc 54th US Rock Mech Symp 28 June - 1 July.* 2020. <https://www.onepetro.org/conference-paper/ARMA-2020-1626>.
30. Lian G, Thornton C, Icdtui D. *Trubal a 3-D Computer Program for Modelling Particle Assemblies*. 1998.
31. Thornton C. *Granular Dynamics, Contact Mechanics and Particle System Simulations*. Vol 24. Cham: Springer International Publishing; 2015. <http://dx.doi.org/10.1007/978-3-319-18711-2>.
32. Hertz H. Über die Berührung fester elastischer Körper. *J für die reine und Angew Math.* 1881;171:156–171.
33. Rakhimzhanova AK, Thornton C, Minh NH, Fok SC, Zhao Y. Numerical simulations of triaxial compression tests of cemented sandstone. *Comput Geotech.* 2019;113(May):103068. <http://dx.doi.org/10.1016/j.compgeo.2019.04.013>.
34. Khamitov F, Minh NH, Zhao Y, Fok SC. Implementation of jkr contact model in liggghts. 2019:9. <https://mercurylab.co.uk/dem8/wp-content/uploads/sites/4/2019/07/103.pdf>.
35. Norouzi HR, Zarghami R, Sotudeh-Gharebagh R, Mostoufi N. *Coupled CFD-DEM Modeling*. Chichester, UK: John Wiley & Sons, Ltd; 2016. <http://dx.doi.org/10.1002/9781119005315>.
36. Zhou ZY, Kuang SB, Chu KW, Yu AB. Discrete particle simulation of particle–fluid flow: model formulations and their applicability. *J Fluid Mech.* 2010;661:482–510. <http://dx.doi.org/10.1017/S002221201000306X>.
37. Di Felice R. The voidage function for fluid–particle interaction systems. *Int J Multiph Flow.* 1994;20(1):153–159. [http://dx.doi.org/10.1016/0301-9322\(94\)90011-6](http://dx.doi.org/10.1016/0301-9322(94)90011-6).
38. Kozhagulova A, Shabdirova A, Minh NH, Zhao Y. An integrated laboratory experiment of realistic diagenesis, perforation and sand production using a large artificial sandstone specimen. *J Rock Mech Geotech Eng.* 2020. <http://dx.doi.org/10.1016/j.jrmge.2020.09.004>.
39. Shabdirova AD, Bisikenova Z, Minh NH, Kim JR. Sample preparation method of clay-rich sandstone analogue of sandstone reservoirs in Kazakhstan. In: *50th US Rock Mech / Geomech Symp 2016*, vol. 2; 2016:904–910.
40. Oryem M, Arroyo M, Butlanska J, Gens A. DEM modelling of cone penetration tests in a double-porosity crushable granular material. *Comput Geotech.* 2016;73:109–127. <http://dx.doi.org/10.1016/j.compgeo.2015.12.001>.
41. O'Connor RM, Torczynski JR, Preece DS, Klosek JT, Williams JR. Discrete element modeling of sand production. *Int J Rock Mech Min Sci.* 1997;34(3–4):231. e1–231.e15. [http://dx.doi.org/10.1016/S1365-1609\(97\)00198-6](http://dx.doi.org/10.1016/S1365-1609(97)00198-6).
42. Shabdirova A, Minh NH, Zhao Y. A sand production prediction model for weak sandstone reservoir in Kazakhstan. *J Rock Mech Geotech Eng.* 2019;11(4):760–769. <http://dx.doi.org/10.1016/j.jrmge.2018.12.015>.
43. Risnes R, Bratli RK, Horsrud P. Sand stresses around a wellbore. *Soc Pet Eng J.* 1982;22(06):883–898. <http://dx.doi.org/10.2118/9650-PA>.
44. Daigle H, Rasromani E, Gray KE. Near-wellbore permeability alteration in depleted, anisotropic reservoirs. *J Pet Sci Eng.* 2017;157(July):302–311. <http://dx.doi.org/10.1016/j.petrol.2017.07.046>.
45. Li Y, Xu Y, Thornton C. A comparison of discrete element simulations and experiments for sandpiles composed of spherical particles. *Powder Technol.* 2005;160(3):219–228. <http://dx.doi.org/10.1016/j.powtec.2005.09.002>.
46. Polillo A, Graves RM. *Simulation of Sand Arching Mechanics using an Elasto-Plastic Finite Element Formulation this Paper Presents a Method to Simulate Sand Production Mechanics using an George D. Vassilellis*. SPE, Richardson Operating Company James W. Crafton; 1994 SPE © 1994. <http://dx.doi.org/10.2118/23728-PA>.
47. Risnes R, Bratli RK, Horsrud P. Sand arching - A case study. SPE. 1982. <http://dx.doi.org/10.2118/12948-MS>.
48. Hall CD, Harrisberger WH. Stability of sand arches: A key to sand control. *J Pet Technol.* 1970;22(07):821–829. <http://dx.doi.org/10.2118/2399-PA>.
49. Wu B, Choi SK, Denke R, et al. A new and practical model for amount and rate of sand production estimation. In: *Offshore Technology Conference Asia*. Offshore Technology Conference; 2016. <http://dx.doi.org/10.4043/26508-MS>.
50. Shabdirova A, Minh NH, Zhao Y, Fok SC. The role of plastic zone permeability in sand production in weak sandstone reservoirs. *Undergr Space Under Rev.* 2020.